Journal of Hazardous Materials 185 (2011) 889–897

Contents lists available at ScienceDirect

Journal of Hazardous Materials

journal homepage: www.elsevier.com/locate/jhazmat

Synthesis of hierarchical $Ni(OH)_2$ and NiO nanosheets and their adsorption kinetics and isotherms to Congo red in water

Bei Cheng, Yao Le, Weiquan Cai, Jiaguo Yu*

State Key Laboratory of Advanced Technology for Material Synthesis and Processing, Wuhan University of Technology, Luoshi Road 122#, Wuhan 430070, PR China

ARTICLE INFO

Article history:
Received 31 May 2010
Received in revised form 7 September 2010
Accepted 28 September 2010
Available online 7 October 2010

Keywords:
$Ni(OH)_2$
NiO
Nanosheets
Hierarchical porous structures
Congo red
Adsorption isotherm
Kinetics

ABSTRACT

$Ni(OH)_2$ and NiO nanosheets with hierarchical porous structures were synthesized by a simple chemical precipitation method using nickel chloride as precursors and urea as precipitating agent. The as-prepared samples were characterized by X-ray diffraction, scanning electron microscopy and nitrogen adsorption–desorption isotherms. Adsorption of Congo red (CR) onto the as-prepared samples from aqueous solutions was investigated and discussed. The pore structure analyses indicate that $Ni(OH)_2$ and NiO nanosheets are composed of at least three levels of hierarchical porous organization: small mesopores (ca. 3–5 nm), large mesopores (ca. 10–50 nm) and macropores (100–500 nm). The equilibrium adsorption data of CR on the as-prepared samples were analyzed by Langmuir and Freundlich models, suggesting that the Langmuir model provides the better correlation of the experimental data. The adsorption capacities for removal of CR was determined using the Langmuir equation and found to be 82.9, 151.7 and 39.7 mg/g for $Ni(OH)_2$ nanosheets, NiO nanosheets and NiO nanoparticles, respectively. Adsorption data were modeled using the pseudo-first-order, pseudo-second-order and intra-particle diffusion kinetics equations. The results indicate that pseudo-second-order kinetic equation and intra-particle diffusion model can better describe the adsorption kinetics. The as-prepared $Ni(OH)_2$ and NiO nanosheets are found to be effective adsorbents for the removal of Congo red pollutant from wastewater as a result of their unique hierarchical porous structures and high specific surface areas.

1. Introduction

In recent years, materials with hierarchically multimodal pore-size distributions have attracted a growing attention, because they combine the benefits of high surface area micro- and mesoporosity with the accessible diffusion pathways of macroporous networks and play key roles in industrial processes, from adsorption to catalysis, catalytic supports, gas storage, purification, and separation [1–4]. The controlled synthesis of hierarchically nanoporous materials such as NiO [5,6], TiO_2 [7,8], WO_3 [9,10], and Al_2O_3 [11–13] has led to higher adsorption and catalytic efficiency. Some methods including soft- and hard-templating synthesis, chemically induced self-transformation and precipitation in the presence of ammonia, urea and metal salts have been used to prepare hierarchically porous structured metal oxides [11–16]. The formation of hierarchical structures is widely considered to be due to a self-assembly process, in which building blocks, i.e., nanoparticles (0D), nanofibers, nanowires and nanoribbons (1D), nanosheets and nanofilms (2D) self-assemble into order higher level structures with various morphologies [13,17,18]. However, it is still a great challenge to develop simple, environmentally friendly and versatile methods for the synthesis of hierarchically structured metal oxides with designed chemical components and textures, which could greatly facilitate their future applications.

Various kinds of synthetic dyestuffs appear in the effluents of wastewater in some industries such as dyestuff, textiles, leather, paper, plastics, etc. [19]. The colored effluents of waste from these industries can be mixed in surface water and ground water systems, and then they may bring a chief threat to human health due to either toxic or mutagenic and carcinogenic for most of dyes [20]. Therefore, it is necessary to remove the dye pollutions. Congo red is an example of anionic diazo dyes and is prepared by coupling tetrazotised benzidine with two molecules of napthionic acid. It is the first synthetic dye produced that is capable of dying cotton directly. Congo red containing effluents are generated from textiles, printing and dyeing, paper, rubber plastics industries, etc. Due to its structural stability, it is difficult to biodegrade. Physico-chemical or chemical treatment of such wastewaters is, however, possible. Adsorption is considered to be an attractive option in treating such wastewater [21–26]. Adsorption using activated carbon is a common and popular method, because this method has considerable potential for the purification of wastewater due to its low process

* Corresponding author. Tel.: +86 27 87871029; fax: +86 27 87879468.
E-mail address: jiaguoyu@yahoo.com (J. Yu).

0304-3894/$ – see front matter © 2010 Elsevier B.V. All rights reserved.
doi:10.1016/j.jhazmat.2010.09.104

costs and relatively efficient dye removal. However, activated carbon has some drawbacks such as slow adsorption kinetics and low adsorption capacity of bulky adsorbates due to the microporous nature of activated carbon. Therefore, adsorbents should have a high surface area with large pores as well as selective adsorption sites [27–30]. In addition, wastewater containing anionic dyes such as Congo red often contains other cationic and neutral pollutants, and the presence of large amounts of these pollutants in wastewater sometimes reduces the effectiveness of anionic dyes removal using the adsorbents because the sorption of cationic and neutral dye pollutants depress the sorption capacity and efficiency of adsorbents [31]. Therefore, it is very important to find new adsorbents with high selectivity to anionic dyes for the versatile treatment of wastewater.

Nickel hydroxide ($Ni(OH)_2$), as one of the most important transition metal hydroxides, has received more and more attention because of its wide applications. Nickel oxide (NiO) is a very important functional oxide, and it has been widely used in various fields, including catalysis, battery cathodes, electrochromic films and fuel cell electrodes. Therefore, many literatures have reported the synthesis of $Ni(OH)_2$ and NiO with hierarchical nanostructures [32–34]. For example, Wang et al. reported fabrication of hollow spheres and thin films of nickel hydroxide and nickel oxide with hierarchical structures using styrene–acrylic acid copolymer (PSA) latex particles as templates [32]. Yang et al. prepared hierarchical β-$Ni(OH)_2$ and NiO carnations assembled from nanosheet building blocks via a hydrothermal method in mixed solvents of water and glycerol [33]. Zhu et al. synthesized three-dimensional (3D) flower-like hierarchical β-$Ni(OH)_2$ hollow architectures by a facile hydrothermal route in mixed solvents of water and ethanol. Furthermore, the feasibility of $Ni(OH)_2$ and NiO nanomaterials for their application in water treatment is also reported and evaluated [35,36]. In our previous work, we reported the synthesis of boehmite hollow core–shell and hollow microspheres via sodium tartrate-mediated phase transformation and their enhanced adsorption performance for removal of Congo red and phenol [12]. Very recently, we further reported template-free synthesis of hierarchical spindle-like γ-Al_2O_3 materials and their adsorption affinity towards organic and inorganic pollutants in water [13]. However, the use of hierarchically porous $Ni(OH)_2$ and NiO as adsorbents in water treatment has been rarely studied [36]. Herein, we report the template-free synthesis of hierarchical porous $Ni(OH)_2$ and NiO materials from $NiCl_2$ and urea via a facile hydrothermal reaction–precipitation route and their potential application for the removal of Congo red.

2. Experimental

2.1. Sample preparation

All reagents used in the experiments were in analytical grade (purchased from Shanghai Chemical Industrial Company) and used without further purification. Distilled water was used for all synthesis and treatment processes.

The preparation of $Ni(OH)_2$ nanosheets was performed as follows. Typically, 0.00024 mol of $NiCl_2$ and 0.0048 mol of urea were dissolved in 100 mL of distilled water. After the mixture was stirred for 10 min, the mixed solution was kept at 90 °C for 48 h. Finally, the precipitates were washed three times with water and ethanol, respectively, and dried at 80 °C for 6 h to obtain $Ni(OH)_2$ nanosheets. The dried sample was labeled sample A (see Table 1). To obtain NiO nanosheets, the as-prepared sample A were heated to 300 °C at a rate of 1 °C min^{-1} in air and kept at 300 °C for 5 h. The calcined product was labeled sample B. The NiO reagent, obtained from Shanghai Chemical Industrial Company, was labeled sample C. The detailed physical parameters for samples A, B and C are shown in Table 1.

Table 1
Physical properties of the samples.

No.	Compositions	Morphology	Crystallinite size (nm)	Pore volume (cm^3/g)	S_{BET} (m^2/g)
A	$Ni(OH)_2$	Nanosheets	8.1	0.21	127
B	NiO	Nanosheets	5.5	0.28	201
C	NiO reagents	Nanoparticles	46.3	0.008	2.5

2.2. Characterization

The X-ray diffraction (XRD) measurements, which were used to characterize the crystalline phase and crystallite size of the $Ni(OH)_2$ and NiO nanosheets, were carried out on an X-ray diffractometer (type HZG41B-PC) using Cu Kα radiation at a scan rate of 0.05°2θ s^{-1}. The accelerating voltage and applied current were 40 kV and 80 mA, respectively. The average crystallite size of $Ni(OH)_2$ and NiO was quantitatively calculated using Scherrer formula ($d = 0.9\lambda/B\cos\theta$, where d, λ, B and θ are crystallite size, Cu Kα wavelength (0.15418 nm), full width at half maximum intensity (FWHM) of $Ni(OH)_2$ (0 0 3) and NiO (1 1 1) peaks in radians and Bragg's diffraction angle, respectively) after correcting the instrumental broadening. Scanning electron microscopy (SEM) was performed by an S-4800 Field Emission SEM (FESEM, Hitachi, Japan) at an accelerating voltage of 10 kV and linked with an Oxford Instruments X-ray analysis system. The Brunauer–Emmett–Teller (BET) specific surface area (S_{BET}) of the powders was analyzed by nitrogen adsorption in a Micromeritics ASAP 2020 nitrogen adsorption apparatus (USA). All the as-prepared samples were degassed at 100 °C prior to nitrogen adsorption measurements. The BET surface areas were determined by a multipoint BET method using the adsorption data in the relative pressure (P/P_0) range of 0.05–0.3. A desorption isotherm was used to determine the pore-size distribution by the Barret–Joyner–Halender (BJH) method, assuming a cylindrical pore model. The nitrogen adsorption volume at the relative pressure (P/P_0) of 0.994 was used to determine the pore volume and average pore size.

2.3. Adsorption equilibrium and kinetic experiments

Adsorption isotherm experiments were carried out by adding a fixed amount of adsorbent (5 mg) to a series of 100 mL beakers filled with 25 mL diluted Congo red (CR) solutions (15–50 mg/L) at natural pH (ca. 7). The beakers were then sealed and stirred for 12 h at room temperature. The effect of pH was investigated at room temperature and initial concentration 15 mg/L. pH adjustments were done using solutions of 0.1 M NaOH and 0.1 M HCl. The beakers were then removed from the stirrer, and the final concentration of CR in the solution was measured at maximum absorption wavelengths of CR (498 nm) using UV/vis spectrophotometer (Shimadzu UV/vis 2550 Spectrophotometer, Japan). The amount of CR at equilibrium q_e (mg/g) on the adsorbent samples was calculated from the following equation:

$$q_e = \frac{(C_0 - C_e)V}{W} \quad (1)$$

where C_0 and C_e (mg/L) are the liquid phase concentrations of CR at initial and equilibrium, respectively, V is the volume of the solution (L) and W is the mass of adsorbent used (g).

The adsorption kinetic experiments were basically identical to those of isotherm experiments. The aqueous samples were taken to pre-set time intervals and the concentrations of CR were simi-

larly measured. The amount of adsorption at time t, q_t (mg/g), was calculated by:

$$q_t = \frac{(C_0 - C_t)V}{W} \quad (2)$$

where C_0 and C_t (mg/L) are the liquid phase concentrations of CR at initial and any time t, respectively, V is the volume of the solution (L) and W is the mass of adsorbent used (g).

3. Results and discussion

3.1. XRD

XRD was used to characterize the phase structure and crystallite size of the samples A, B and C. Fig. 1a shows XRD pattern of sample A. Quantitative analysis of this pattern shows that all peaks in the pattern can be assigned to the diffraction of (0 0 3), (0 0 6), (1 0 1), and (1 1 0) planes of Rhombohedral α-Ni(OH)$_2$ (JCPDS card no. 38-0715, a = 3.08 Å and c = 23.41 Å), indicating the formation of α-Ni(OH)$_2$ [36–38]. XRD pattern of sample B (Fig. 1b) indicates that compared with Fig. 1a, new peaks appear, which can be attributed to cubic NiO phase with lattice constant a = 4.1946 Å (JCPDS No. 65-2901, space group: *Fm*-3*m* (225)) [39,40]. The broad diffraction peaks of samples A and B suggest that the crystallite sizes of the Ni(OH)$_2$ and NiO samples are small and the corresponding crystallite sizes, calculated by Scherrer formula, are 8.1 and 5.5 nm, respectively. The sharp diffraction peaks of sample C suggest that sample C is composed of large grains and the corresponding crystallite size is about 46.3 nm (see Table 1).

3.2. SEM

The morphology and microstructure of the samples were observed by SEM (Fig. 2). SEM image shows that Ni(OH)$_2$ powders are highly porous films (Fig. 2a), with a wide size distribution of ca. 2–10 μm and mean thickness of about 1 μm (see inset in Fig. 2b). High-magnification SEM image reveals that the external surface of the films consists of randomly aggregated and interconnecting 10 nm-thick nanosheets (Fig. 2b). As a consequence, the outer surface was extensively roughened in the form of a highly disordered porous superstructure. In contrast, the inner surface of the films (attached beaker) is relatively smooth (see inset in Fig. 2b). Further investigations show that the α-Ni(OH)$_2$ nanosheets can be readily converted into intact NiO nanosheets by calcination at 300 °C (Fig. 2c and d). No large morphology change is observed. The above XRD results indicate that the as-prepared Ni(OH)$_2$ and NiO nanosheet samples consist of 8.1 and 5.5 nm crystallites, respectively. This implies that the observed nanosheets are composed of many smaller crystallites. Contrarily, SEM image indicates that NiO reagent (sample C) contains a large amount of nanoparticles with size of several hundred nm (see Fig. 2e). This indicates that the particle size of sample C obtained by SEM observation is obviously bigger than the crystallite size (46.3 nm) determined by the XRD. This is not surprising because the particle size observed by SEM is the size of secondary (or aggregated) particles.

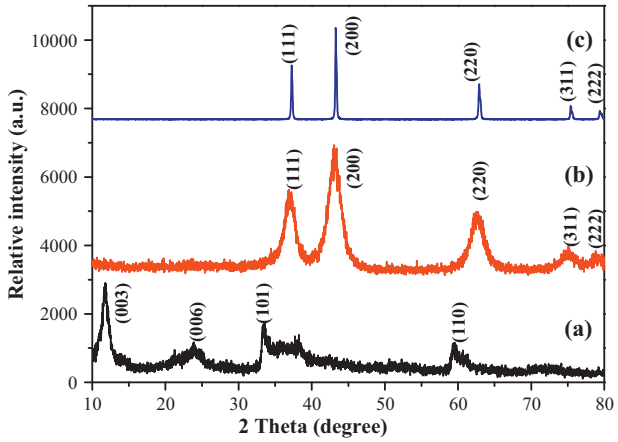

Fig. 1. XRD patterns of samples A (a), B (b) and C (c).

3.3. Specific surface areas and porosity

To characterize the specific surface areas and porosity of the as-prepared samples A and B, N_2 adsorption analysis was carried out. Fig. 3a and b, respectively, presents the N_2 adsorption–desorption isotherms and the corresponding pore-size distribution curves for the A and B samples. The desorption branches of the isotherms show a stepwise behavior and ends at the limiting pressure of the hysteresis closure, implying non-uniformity of pore openings associated with pore constrictions and/or ink-bottle pores with narrow necks [31,41]. The hysteresis loop in the relative pressure range between 0.4 and 0.9 is probably related to the pores present within nanosheets, which are formed between primary crystallites. The high-pressure parts of the hysteresis loop ($0.9 < P/P_0 < 1$) are probably associated with textural larger pores that can be formed between secondary particles due to aggregation of nanoflakes into the flower-like superstructures. As can be seen from Fig. 3b, the pore-size distribution curves are quite broad and bimodal with small mesopores (peak pore at ca. 4.0 nm) and larger ones (peak pore at ca. 45 nm). The smaller mesopores reflects porosity in nanoflakes, while larger mesopores can be related to the pores formed between stacked nanoflakes. The macroporous structure (ca. 100–500 nm) can be directly observed on the SEM images of samples A and B shown in Fig. 2, which cannot be accessed by N_2 adsorption–desorption analysis. As mentioned above, the A and B samples exhibit a disordered slit-like macroporous framework created by stacking nanoflakes. Their unique three-dimensional macroporous framework is well suited for adsorption and introducing reactive molecules into the interior space of the samples [41]. The BET specific surface areas of samples A and B are 127 and 201 m^2/g, respectively, indicating that the samples have the relatively high surface-to-volume ratio. Usually, for adsorbent, a large surface area can offer more active adsorption sites. The hierarchical macro-/mesoporous structures are beneficial to enhance the adsorption efficiency of adsorbate molecules and their flow rates [3,41].

3.4. Adsorption kinetics

The adsorption kinetics is important for adsorption studies because it can predict the rate at which a pollutant is removed from aqueous solutions and provides valuable data for understanding the mechanism of sorption reactions [42]. Fig. 4 shows the kinetics of CR adsorption on the samples A, B and C obtained by batch contact time studies for an initial CR concentration of 25 mg/L at pH 7.0. As expected, for samples A and B, the adsorptions are very fast during the first 10 min, and the equilibrium is achieved within 300 min. In addition, under the same experimental conditions used, the adsorption capacities were much different for the samples A, B and C. Sample B has the highest capacity, and then sample A, and finally sample C. The fast CR uptake indicates a high complexation rate between the dye molecules and adsorbent, which is related to their small primary crystallite size of adsorbents and high specific surface areas, pore volume and porous structures as presented in Table 1, Figs. 2 and 3. The above results also suggest that the smaller the crystallite size, the larger the specific surface areas, the more the adsorption or active sites, the faster the adsorption rates are.

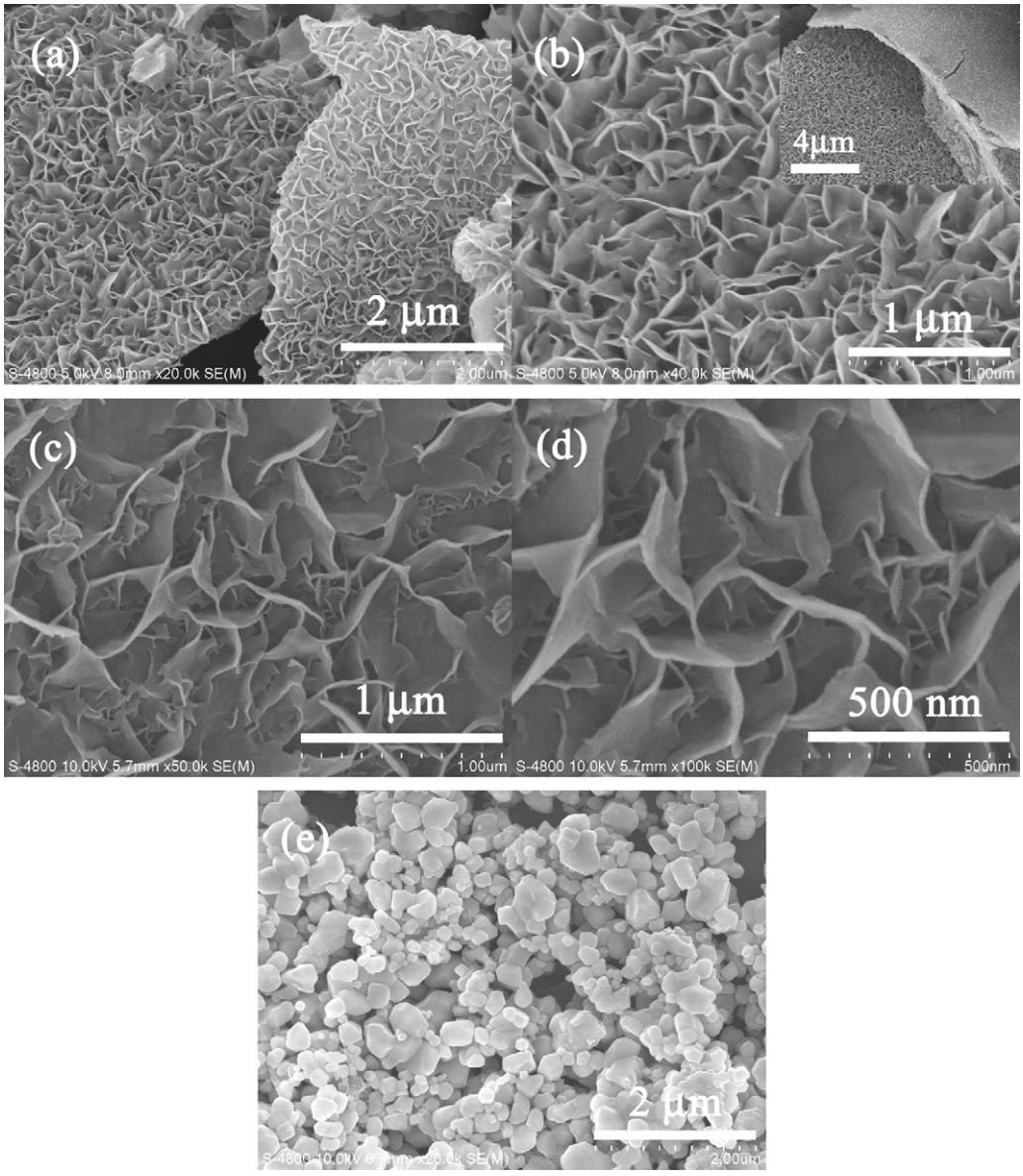

Fig. 2. SEM images of samples A (a and b), B (c and d) and C (e).

Therefore, the equilibrium is rapidly achieved. The fast sorption represents an advantage for water treatment system design.

Three known kinetic models are used to investigate the mechanism of the adsorption [43,44]. Firstly, pseudo-first-order equation has been widely used for analyzing the adsorption of an adsorbate from an aqueous solution.

$$\log(q_e - q_t) = \log q_e - \frac{k_1}{2.303}t \quad (3)$$

where q_e and q_t are the amounts of CR adsorbed (mg/g) at equilibrium and at time t (min), respectively, and k_1 (min^{-1}) is the rate constant adsorption. Values of k_1 are calculated from the plots of log ($q_e - q_t$) versus t (see Fig. 5a) for samples A and B. The R^2 values obtained are relatively small and the experimental q_e values do not agree with the calculated values obtained from the linear plots (Table 2).

Secondly, the pseudo-second-order equation based on equilibrium adsorption is expressed as follows [43]:

$$\frac{t}{q_t} = \frac{1}{k_2 {q_e}^2} + \frac{1}{q_e}t \quad (4)$$

where k_2 (g/mg min) is the rate constant of second-order adsorption. The linear plot of t/q_t versus t is shown in Fig. 5b and the obtained R^2 values are greater than 0.999 for samples A, B and C. It also shows a good agreement between the experimental and the calculated q_e values (Table 3), indicating the applicability of this model to describe the adsorption process of CR onto the prepared samples.

As the above two kinetic models were not able to explain the diffusion mechanism, thus intra-particle diffusion kinetic model based on the theory or equation proposed by Weber and Morris is tested [45], which is an empirically functional relationship, common to the most adsorption processes. The adsorbate uptake varies almost proportionally with $t^{1/2}$ rather than with the contact time t. According to the following Weber-Morris's equation:

$$q_t = k_{di}\sqrt{t} + c_i \quad (5)$$

where k_{di} is the rate parameter of stage i (mg/g $h^{1/2}$), calculated from the slope of the straight line of q_t versus $t^{1/2}$. C_i is the intercept of stage i, giving an idea about the thickness of boundary layer, i.e., the larger the intercept, the greater the boundary layer effect is. For

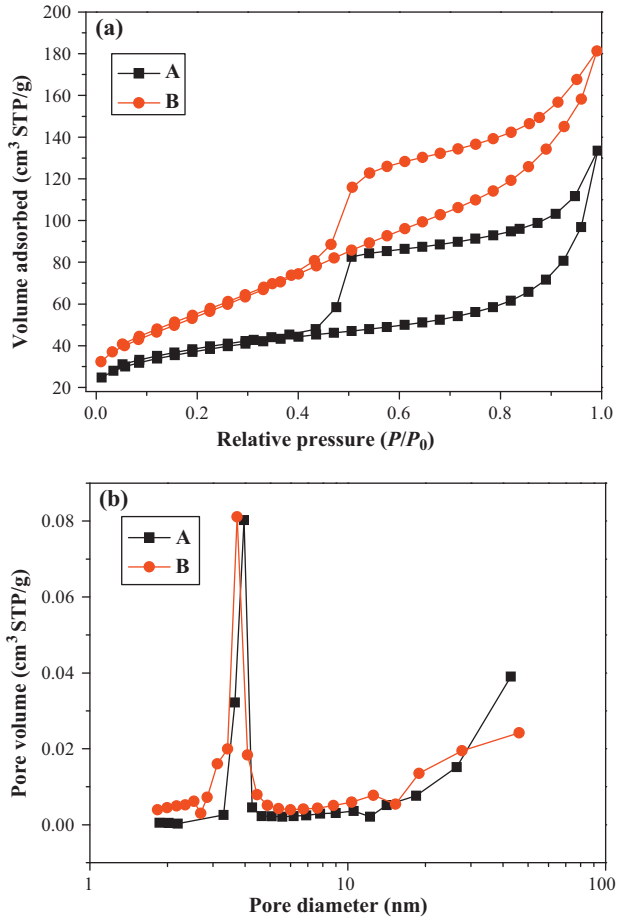

Fig. 3. Pore-size distribution curves (a) and the corresponding nitrogen adsorption–desorption isotherms (b) of sample A and B.

intra-particle diffusion, q_t versus $t^{1/2}$ will be linear and if the plot passes through the origin, then the rate-limiting process is only due to the intra-particle diffusion [43,46].

Fig. 5c presents a linear fit of intra-particle diffusion model for adsorption of CR onto samples A and B. Such types of plots present multilinearity, indicating that two or more steps take place. The first, sharper region is the instantaneous adsorption or external surface adsorption stage, which was completed within the first 10 min. This is not surprising because the high initial CR concentration is driving force of diffusion. The second region is the gradual or slow adsorption stage where intra-particle diffusion is the rate-limiting step. The third region is the final equilibrium stage where intra-particle diffusion further slows down due to the extremely low concentrations of adsorbate left in the solutions [43]. It is evident that the rate of external surface adsorption (stage 1) with sample B is higher than that with samples A and C for the adsorption of CR (Table 4). Stage 1 is rapidly completed within about 10 min and the stage of intra-particle diffusion control (stage 2) is then attained. As discussed above, CR is slowly transported via

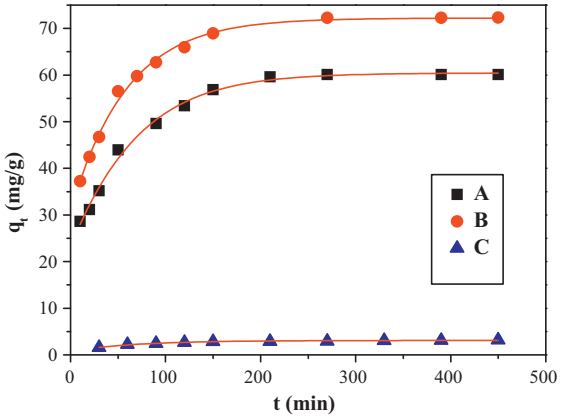

Fig. 4. The variation of adsorption capacity with adsorption time for CR on samples A, B and C (T = 25 °C; adsorbent dose = 200 mg/L; CR concentration = 25 mg/L and pH 7).

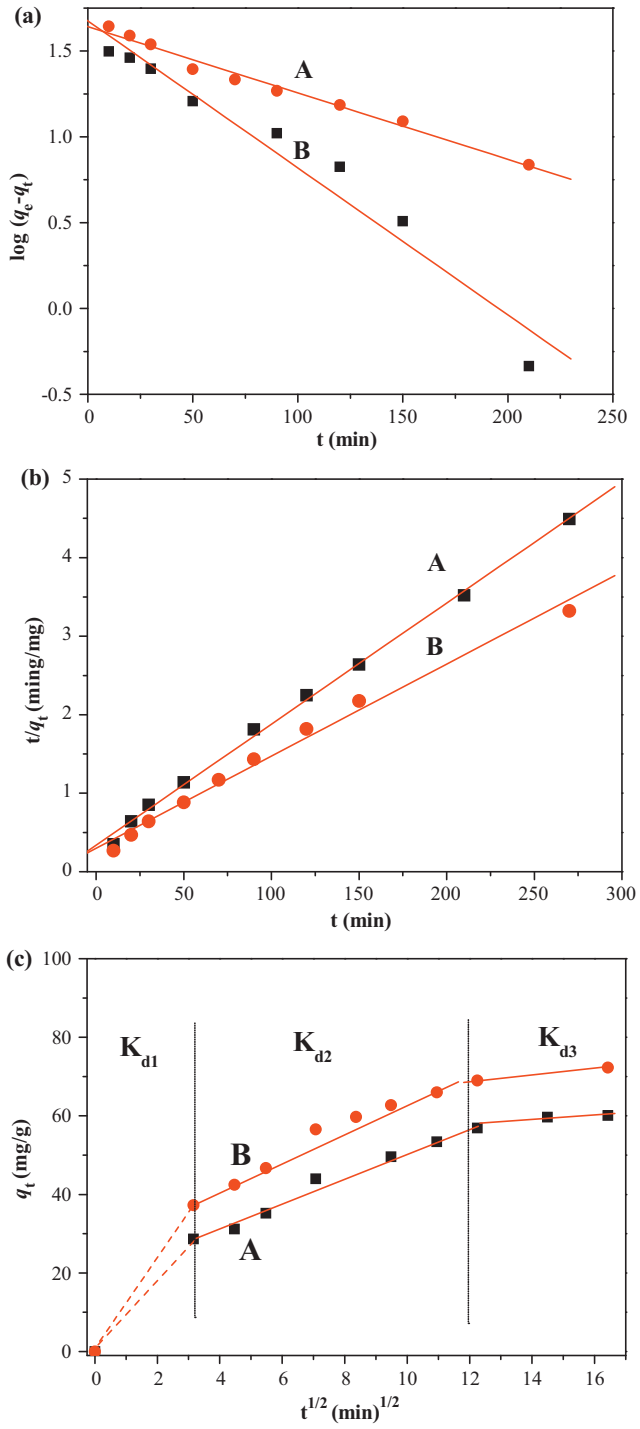

Fig. 5. Pseudo-first-order kinetics (a), second-order kinetics (b) and intra-particle diffusion kinetics (c) for adsorption of CR onto samples A and B (T = 25 °C; adsorbent dose = 200 mg/L; CR concentration = 25 mg/L and pH 7).

Table 2
Pseudo-first-order adsorption kinetic constants of samples A, B and C.

Samples	C_0 (mg/L)	$q_{e,exp}$ (mg/g)	Pseudo-first-order model			
			$q_{e,cal}$ (mg/g)	K_1 ($\times 10^{-3}$ min^{-1})	R^2	S.D. (%)
A	25	60.10	47.35	82.56	0.978	8.7
B		72.31	41.47	7.83	0.979	15.1
C		3.18	1.60	3.73	0.988	20.3

Table 3
Pseudo-second-order adsorption kinetic constants of samples A, B and C.

Samples	C_0 (mg/L)	$q_{e,exp}$ (mg/g)	Pseudo-second-order model			
			$q_{e,cal}$ (mg/g)	K_2 ($\times 10^{-4}$ g/mg min^{-1})	R^2	S.D. (%)
A	25	60.10	64.85	7.05	0.999	3.23
B		72.31	76.28	7.81	0.999	4.09
C		3.18	3.36	9.72	1	2.28

intra-particle diffusion into the particles and is finally retained in hierarchical nanopores. The rate parameters for CR (Table 4) show that the value of k_{d1} and k_{d2} with sample B is larger than that with sample A or C. This is because sample B has a larger surface area and pore volume for solute adsorption instantaneously. Further observation indicates $k_{d1} > k_{d2} > k_{d3}$. This is easy to understand because the concentration of CR left in the solutions gradually decreases.

Normalized standard deviation, S.D. (%), is used to find the most applicable model that could describe the kinetic study of adsorption of CR dye on the samples A, B and C. The normalized standard deviation S.D. (%) was calculated using the following equation:

$$\text{S.D.}(\%) = 100 \times \left\{ \sum \frac{[(q_{e,exp} - q_{e,cal})/q_{e,exp}]^2}{N-1} \right\}^{1/2} \quad (6)$$

where n is the number of data points, $q_{t,exp}$ the experimental values and $q_{e,cal}$ is the calculated value by the above three models. Based on the values of S.D. (%) given in Tables 2–4, it is clear that pseudo-second-order equation and intra-particle diffusion model are better in describing the adsorption kinetics of CR using samples A, B and C [44,46].

3.5. Adsorption isotherms

Adsorption capacity at different aqueous equilibrium concentration can be illustrated by the adsorption isotherm. Fig. 6 shows adsorption isotherms for CR on samples A and B at pH 7 and 25 °C. The adsorption process is normally described by the Langmuir and the Freundlich isotherms. The Langmuir equation assumes that there is no interaction between the adsorbate molecules and that the sorption is localized in a monolayer. It is then assumes that once a dye molecule occupies a site, no further adsorption can take place at that site. The Langmuir equation is expressed as follows [47]:

$$q_e = \frac{q_{max} K_L C_e}{1 + K_L C_e} \quad (7)$$

where C_e is the equilibrium concentration of CR in solution (mg/L), q_e is the equilibrium capacity of CR on the adsorbent (mg/g), q_{max} is the maximum adsorption capacity of the adsorbent corresponding

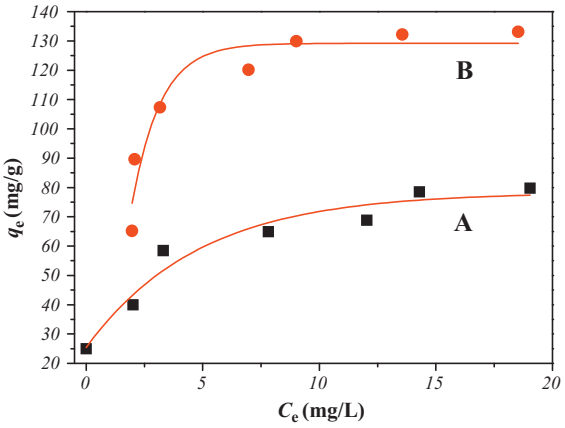

Fig. 6. Adsorption isotherms for CR on samples A and B (T = 25 °C; adsorbent dose = 200 mg/L; CR concentration = 15–50 mg/L and pH 7).

to complete monolayer coverage on the surface (mg/g), and K_L is the Langmuir adsorption constant (L/mg) and related to the free energy of adsorption. Eq. (7) can be rearranged to a linear form:

$$\frac{C_e}{q_e} = \frac{1}{q_{max} K_L} + \frac{C_e}{q_{max}} \quad (8)$$

The constants q_{max} and K_L can be calculated from the intercepts and the slopes of the linear plots of C_e/q_e versus C_e (Fig. 7). It can be observed that the equilibrium adsorption data follow Langmuir's isotherm. Conformation of the experimental data into Langmuir isotherm model indicates the homogeneous nature of sample surface, i.e., each dye molecule/adsorbent adsorption has equal adsorption activation energy and demonstrates the formation of monolayer coverage of CR molecule on the outer surface of adsorbent. Langmuir parameters calculated from Eq. (8) are listed in Table 5.

The essential characteristics of the Langmuir equation can be expressed in term of a dimensionless separation factor, R_L, defined

Table 4
Intra-particle diffusion model constants and correlation coefficients for adsorption of Congo red on samples A, B and C.

No.	C_0 (mg/L)	Intra-particle diffusion model								
		K_{d1} (mg/g min$^{1/2}$)	K_{d2} (mg/g min$^{1/2}$)	K_{d3} (mg/g min$^{1/2}$)	C_1	C_2	C_3	$(R_1)^2$	$(R_2)^2$	$(R_3)^2$
A	25	9.06	2.59	0.24	0	22.39	56.20	1.00	0.971	1.00
B		11.79	2.78	0.80	0	32.93	59.22	1.00	0.949	1.00
C		0.29	0.09	0.04	0	1.48	2.38	1.00	0.915	1.00

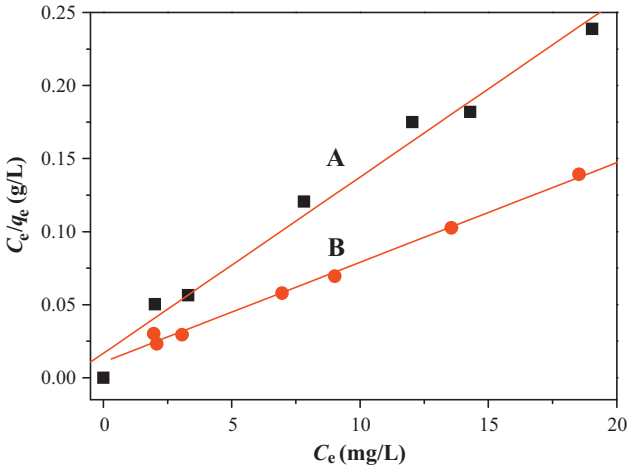

Fig. 7. Langmuir isotherms for CR adsorption onto samples A and B at 25 °C.

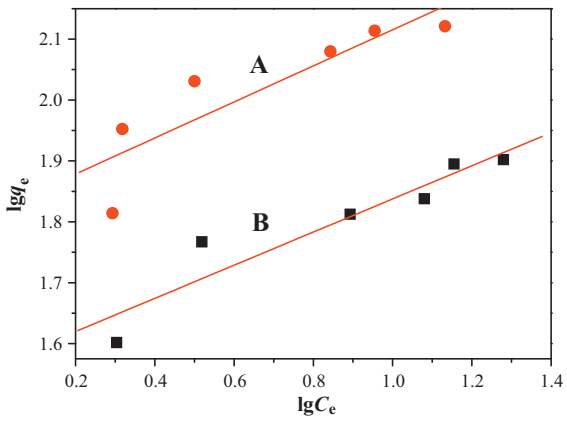

Fig. 8. Freundlich isotherm for CR adsorption onto samples A and B at 25 °C.

as follows [48]:

$$R_L = \frac{1}{1 + K_L C_0} \quad (9)$$

where C_0 is the highest initial solute concentration and K_L is the Langmuir's adsorption constant (L/mg). Table 5 shows the values of R_L (0.027–0.22) are in the range of 0–1, confirming the favorable uptake of the CR dye.

The Freundlich adsorption model assumes that adsorption takes place on heterogeneous surfaces. The Freundlich equation is an empirical equation and can be written as follows [49]:

$$q_e = K_F C_e^{1/n} \quad (10)$$

where q_e is the solid phase adsorbate concentration in equilibrium (mg/g), C_e the equilibrium liquid phase concentration (mg/L), K_F the Freundlich constant (mg/g)(L/mg)$^{1/n}$ and $1/n$ is the heterogeneity factor. A linear form of the Freundlich expression can be obtained by taking logarithms of Eq. (10):

$$\ln q_e = \ln K_F + \frac{1}{n} \ln C_e \quad (11)$$

Therefore, a plot of $\ln q_e$ versus $\ln C_e$ (Fig. 8) enables the constant K_F and exponent $1/n$ to be determined. The Freundlich isotherm describes reversible adsorption and is not restricted to the formation of the monolayer. The Freundlich equation predicts that the CR concentration on the adsorbent will increase so long as there is an increased in the CR concentration in the liquid. It is clear from Table 5 that the values of the Freundlich exponent n were greater than 1 values, $n > 1$ represent favorable adsorption condition [46,50]. The result shows that Freundlich isotherm can fit the equilibrium data for adsorption of CR on the as-prepared samples.

Table 6 lists the comparison of maximum monolayer adsorption capacity of CR onto various adsorbents. The hierarchical porous $Ni(OH)_2$ and NiO prepared in this work have a relatively large adsorption capacity of 82.9 and 151.7 mg/g, respectively, if compared with some data obtained from the literatures.

Table 6
Comparison of the maximum monolayer adsorption of CR onto various adsorbents.

Adsorbents	Maximum monolayer adsorption capacity (mg/g)	References
Hierarchical $Ni(OH)_2$ nanosheets	82.9	This work
Hierarchical NiO nanosheets	151.7	This work
Reagent NiO nanoparticles	39.7	This work
Single-crystalline NiO nanosheets	36.1	[33]
NaBentonite (Clay materials)	35.84	[22]
Kaolin (Clay materials)	5.44	[22]
Zeolite (Clay materials)	3.77	[22]
Bottom ash	2.05	[47]
Deoiled soya	15.55	[47]

3.6. Effect of pH and selective adsorption

The pH of the CR solution is an important parameter influencing the adsorption capacity of CR onto adsorbents. Fig. 9 shows the effects of pH on the adsorption capacity of CR on NiO nanosheets. It can be observed that the adsorption capacity of NiO decreases

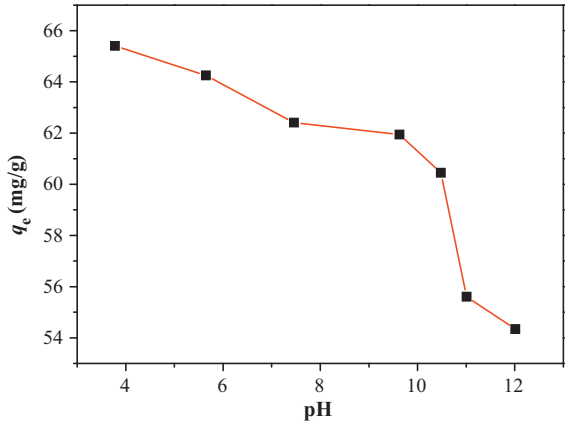

Fig. 9. Effects of pHs on the adsorption capacity of CR onto NiO (sample B) (T = 25 °C; adsorbent dose = 200 mg/L and CR concentration = 15 mg/L).

Table 5
Adsorption isotherm parameters of samples A, B and C.

Samples	Langmuir isotherm model				Freundlich isotherm model		
	q_{max} (mg/g)	K_L (L/mg)	R^2	R_L	K_F (mg/g)(L/mg)$^{1/n}$	n	R^2
A	82.9	0.72	0.992	0.027	36.7	3.67	0.944
B	151.7	0.55	0.995	0.035	65.9	3.38	0.883
C	39.7	0.07	0.947	0.22	7.8	2.52	0.788

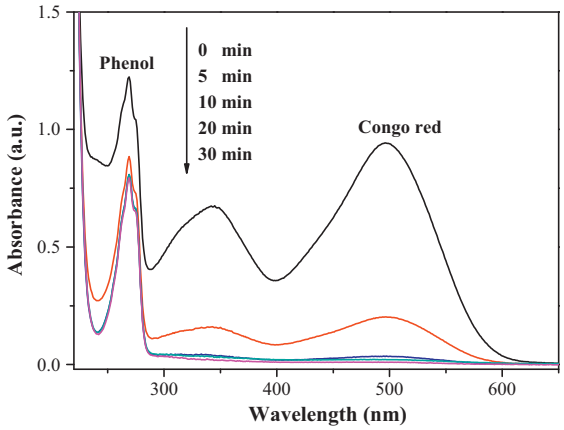

Fig. 10. Selective adsorption property of sample B to CR.

with increasing pH of the CR solution from 4 to 12. The effect of pH can be qualitatively accounted by the pH of CR solution relative to the isoelectric points of NiO [51]. When the pH of the CR solution is below the isoelectric point of NiO (reported values is 10.3) [52], NiO will have a positive surface charge density and would be expected to experience a significant electrostatic attraction to dye molecules with negative surface charge density. CR is the sodium salt of benzidinediazobis-1-naphthylamine-4-sulfonic acid, a kind of anionic dye. This means that the surface of NiO nanosheets is positively charged at pH lower than 10.3, also, with decreasing pH, the surface positive charge density of NiO nanosheets increases. Therefore, it is not surprising that negative CR molecules are easily adsorbed on the NiO surface at a low pH range due to strong electrostatic attraction between CR and NiO. As expected, the lower the pH, the stronger the adsorption is. When the pH of the CR solution is higher than 10.3 (above the isoelectric point of NiO), NiO will have a negative surface charge density. Therefore, adsorption of CR decreases rapidly on the surface of NiO due to the repulse interaction between CR and NiO.

To investigate the selective adsorption of the prepared sample, we add 50 mg of sample A into 25 mL 1.0×10^{-3} M phenol and 25 mL 50 mg/L CR aqueous solution, all the CR are removed from solution after 30 min, while phenol shows no significant decrease (Fig. 10). This is due to the fact that in the neutral solution, the surface of NiO is positively charged, and CR is an anionic dye, then the adsorbents are apt to adsorb CR. On the contrary, phenol is a neutral molecule and is not easily adsorbed by NiO. Further experiments indicate that the adsorption capacity of the as-prepared NiO to anion dyes is much better than cationic and neutral dyes, showing a high selective adsorption [53].

4. Conclusion

$Ni(OH)_2$ and NiO nanosheets with hierarchical porous structures can be synthesized by a simple homogeneous precipitation method without using templates. The as-prepared $Ni(OH)_2$ and NiO powders show trimodal pore-size distributions in the macro-/mesoporous region: fine intrasheet mesopores with peak pore diameters of ca. 4.0 nm, larger intersheet mesopores with peak pore diameters of ca. 45 nm, and macropore with pore diameter of ca. 100–500 nm. Congo red is found to adsorb strongly onto the surface of the $Ni(OH)_2$ and NiO nanosheets. Equilibrium data are fitted by Langmuir and Freundlich isotherms and the equilibrium data are better described by Langmuir isotherm model, with maximum monolayer adsorption capacity of 82.9 and 151.7 mg/g for $Ni(OH)_2$ nanosheets and NiO nanosheets, respectively. The kinetics of the adsorption process is found to follow the pseudo-second-order kinetic model and intra-particle diffusion model. The as-prepared $Ni(OH)_2$ and NiO nanosheets are found to be effective adsorbents for the removal of Congo red pollutant from wastewater as a result of its unique hierarchical porous structure and high specific surface areas.

Acknowledgments

This work was partially supported by the National Natural Science Foundation of China (50625208, 20773097, 20877061 and 51072154). This work was also financially supported by the National Basic Research Program of China (2007CB613302 and 2009CB939704).

References

[1] S.A. Davis, S.L. Burkett, N.H. Mendelson, S. Mann, Bacterial templating of ordered macrostructures in silica and silica-surfactant mesophases, Nature 385 (1997) 420–423.
[2] D. Walsh, L. Arcelli, T. Ikoma, J. Tanaka, S. Mann, Soft templating of metallic and metal oxide porous sponges using sacrificial dextran-based composites, Nat. Mater. 2 (2003) 386–390.
[3] J.G. Yu, Y.R. Su, B. Cheng, Template-free fabrication and enhanced photocatalytic activity of hierarchical macro-/mesoporous titania, Adv. Funct. Mater. 17 (2007) 1984–1990.
[4] J.G. Yu, L.J. Zhang, B. Cheng, Y.R. Su, Hydrothermal preparation and photocatalytic activity of hierarchically sponge-like macro-/mesoporous titania, J. Phys. Chem. C 111 (2007) 10582–10589.
[5] Y.Y. Luo, G.T. Duan, G.H. Li, Synthesis and characterization of flower-like β-$Ni(OH)_2$ nanoarchitectures, J. Solid State Chem. 180 (2007) 2149–2153.
[6] J. Liu, S.F. Du, L.Q. Wei, H.D. Liu, Y.J. Tian, Y.F. Chen, Template-free synthesis of NiO hollow microspheres covered with nanoflakes, Mater. Lett. 60 (2006) 3601–3604.
[7] J.G. Yu, W. Liu, H.G. Yu, A one-pot approach to hierarchically nanoporous titania hollow microspheres with high photocatalytic activity, Cryst. Growth Des. (8) (2008) 930–934.
[8] S.W. Liu, J.G. Yu, S. Mann, Spontaneous construction of photoactive hollow TiO_2 microspheres and chains, Nanotechnology 20 (2009) 325606.
[9] J.G. Yu, L.F. Qi, Template-free fabrication of hierarchically flower-like tungsten trioxide assemblies with enhanced visible-light-driven photocatalytic activity, J. Hazard. Mater. 169 (2009) 221–227.
[10] J.G. Yu, H.G. Yu, H.T. Guo, M. Li, S. Mann, Spontaneous formation of a tungsten trioxide sphere-in-shell superstructure by chemically induced self-transformation, Small (4) (2008) 87–91.
[11] W.Q. Cai, J.G. Yu, S. Mann, Template-free hydrothermal fabrication of hierarchically organized γ-AlOOH hollow microspheres, Micropor. Mesopor. Mater. 122 (2009) 42–47.
[12] W.Q. Cai, J.G. Yu, B. Cheng, B.L. Su, M. Jaroniec, Synthesis of boehmite hollow core/shell and hollow microspheres via sodium tartrate-mediated phase transformation and their enhanced adsorption performance in water treatment, J. Phys. Chem. C (113) (2009) 14739–14746.
[13] W.Q. Cai, J.G. Yu, M. Jaroniec, Template-free synthesis of hierarchical spindle-like γ-Al_2O_3 materials and their adsorption affinity towards organic and inorganic pollutants in water, J. Mater. Chem. 20 (2010) 4587–4594.
[14] J.B. Fei, Y. Cui, X.H. Yan, W. Qi, Y. Yang, K.W. Wang, Q. He, J.B. Li, Controlled preparation of MnO_2 hierarchical hollow nanostructures and their application in water treatment, Adv. Mater. 20 (2008) 452–456.
[15] L.S. Zhong, J.S. Hu, H.P. Liang, A.M. Cao, W.G. Song, L.J. Wan, Self-assembled 3D flowerlike iron oxide nanostructures and their application in water treatment, Adv. Mater. 18 (2006) 2426–2431.
[16] S.Y. Zeng, K.B. Tang, T.W. Li, Z.H. Liang, D. Wang, Y.K. Wang, W.W. Zhou, Hematite hollow spindles and microspheres: selective synthesis, growth mechanisms, and application in lithium ion battery and water treatment, J, Phys. Chem. C 111 (2007) 10217–10225.
[17] Z.X. Fu, W.B. Bu, High efficiency green-luminescent LaPO4: Ce,Tb hierarchical nanostructures: synthesis, characterization, and luminescence properties, Solid State Sci. 10 (2008) 1062–1067.
[18] H.G. Yang, H.C. Zeng, Self-construction of hollow SnO_2 octahedra based on two-dimensional aggregation of nanocrystallites, Angew. Chem. Int. Ed. 43 (2004) 5930–5933.
[19] M.S. Chiou, P.Y. Ho, H.Y. Li, Adsorption of anionic dyes in acid solutions using chemically cross-linked chitosan beads, Dyes Pigments 60 (2004) 69–84.
[20] R. Gong, Y. Ding, M. Li, C. Yang, H. Liu, Y. Sun, Utilization of powdered peanut hull as biosorbent for removal of anionic dyes from aqueous solution, Dyes Pigment 64 (2005) 187–192.
[21] C. Namasivayam, D. Kavitha, Removal of Congo red from water by adsorption onto activated carbon prepared from coir pith, an agricultural solid waste, Dye Pigments 54 (2002) 47–58.
[22] V. Vimonses, S. Lei, B. Jin, C.W.K. Chow, C. Saint, Kinetic study and equilibrium isotherm analysis of Congo red adsorption by clay materials, Chem. Eng. J. 148 (2009) 354–364.

[23] M.K. Purkait, A. Maiti, S. DasGupta, S. De, Removal of Congo red using activated carbon and its regeneration, J. Hazard. Mater. 145 (2007) 287–295.
[24] F. Pavan, S. Dias, E. Lima, E. Benvenutti, Removal of Congo red from aqueous solution by anilinepropylsilica xerogel, Dyes Pigments 76 (2008) 64–69.
[25] I.D. Mall, V.C. Srivastava, N.K. Agarwal, I.M. Mishra, Removal of Congo red from equilibrium isotherm analyses, Chemosphere 61 (2005) 492–501.
[26] H. Chen, J. Zhao, Adsorption study for removal of Congo red anionic dye using organo-attapulgite, Adsorption 15 (2009) 381–389.
[27] K. Nakagawa, A. Namba, S.R. Mukai, H. Tamon, P. Ariyadejwanich, W. Tanthapanichakoon, Adsorption of phenol and reactive dye from aqueous solution on activated carbons derived from solid wastes, Water Res. 38 (2004) 1791–1798.
[28] W. Tanthapanichakoon, P. Ariyadejwanich, P. Japthong, K. Nakarawa, S.R. Mukai, H. Tamon, Adsorption-desorption characteristics of phenol and reactive dyes from aqueous solution on mesoporous activated carbon prepared from waste tires, Water Res. 39 (2005) 1347–1353.
[29] M. Valix, W.H. Cheung, G. McKay, Preparation of activated carbon using low temperature carbonization and physical activation of high ash raw bagasse for acid dye adsorption, Chemosphere 56 (2004) 493–501.
[30] J.B. Joo, J. Park, J. Yi, Preparation of polyelectrolyte-functionalized mesoporous silicas for the selective adsorption of anionic dye in an aqueous solution, J. Hazard. Mater. 168 (2009) 102–107.
[31] S. Kagaya, H. Miyazaki, M. Ito, K. Tohda, T. Kanbara, Selective removal of mercury (II) from wastewater using polythioamides, J. Hazard. Mater. 175 (2010) 1113–1115.
[32] D.B. Wang, C.X. Song, Z.S. Hu, X. Fu, Fabrication of hollow spheres and thin films of nickel hydroxide and nickel oxide with hierarchical structures, J. Phys. Chem. B 109 (2005) 1125–1129.
[33] L.X. Yang, Y.J. Zhu, H. Tong, Z.H. Liang, W.W. Wang, Hierarchical β-$Ni(OH)_2$ and NiO carnations assembled from nanosheet building blocks, Cryst. Growth Des. 7 (2007) 2716–2719.
[34] L.P. Zhu, G.H. Liao, Y. Yang, H.M. Xiao, J.F. Wang, S.Y. Fu, Self-assembled 3D flower-like hierarchical β-$Ni(OH)_2$ hollow architectures and their in situ thermal conversion to NiO, Nanoscale Res. Lett. 4 (2009) 550–557.
[35] X.F. Song, L. Gao, Facile route to nanoporous NiO structures from the alpha-$Ni(OH)_2$/EG Precursor and application in water treatment, J. Am. Ceram. Soc. 91 (2008) 4105–4108.
[36] Z. Song, L.F. Chen, J.C. Hu, R. Richards, NiO(1 1 1) nanosheets as efficient and recyclable adsorbents for dye pollutant removal from wastewater, Nanotechnology 20 (2009) 275707.
[37] P. Jeevanandam, Y. Koltypin, A. Gedanken, Synthesis of nanosized α-nickel hydroxide by a sonochemical method, Nano Lett. 1 (2001) 263–266.
[38] M. Freitas, Nickel hydroxide powder for NiO-OH/$Ni(OH)_2$ electrodes of the alkaline batteries, J. Power Sources 93 (2001) 163–173.
[39] J.X. Ren, Z. Zhou, X.P. Gao, J. Yan, Preparation of porous spherical α-$Ni(OH)_2$ and enhancement of high-temperature electrochemical performances through yttrium addition, Electrochim. Acta 52 (2006) 1120–1126.
[40] B. Zhao, X.K. Ke, J.H. Bao, C.L. Wang, L. Dong, Y.W. Chen, H.L. Chen, Synthesis of flower-like NiO and morphology on its catalytic properties, J. Phys. Chem. C 113 (2009) 14440–14447.
[41] X.X. Yu, J.G. Yu, B. Cheng, M. Jaroniec, Sythesis of hierarchical flower-like AlOOH and TiO_2/AlOOH superstructures and their enhanced photocatalytic properties, J. Phys. Chem. C 113 (2009) 17527–17535.
[42] R.C. Wu, J.H. Qu, Y.S. Chen, Magnetic powder MnO–Fe_2O_3 composite-a novel material for the removal of azo-dye from water, Water Res. 39 (2005) 630–638.
[43] I.A.W. Tan, A.L. Ahmad, B.H. Hameed, Adsorption isotherms, kinetics, thermodynamics and desorption studies of 2,4,6-trichlorophenol on oil palm empty fruit bunch-based activated carbon, J. Hazard. Mater. 164 (2009) 473–482.
[44] Y.S. Ho, G. McKay, Sorption of dye from aqueous solution by peat, Chem. Eng. J. 70 (1998) 115–124.
[45] W.J. Weber, J.C. Morris, Proceedings of the International Conference on Water Pollution Symposium, vol. 2, Pergamon, Oxford, 1962, pp. 231–266.
[46] B.H. Hameed, A.A. Ahmad, N. Aziz, Isotherms, kinetics and thermodynamics of acid dye adsorption on activated palm ash, Chem. Eng. J. 133 (2007) 195–203.
[47] I. Langmuir, Adsorption of gases on plain surfaces of glass mica platinum, J. Am. Chem. Soc. 40 (1918) 1361–1403.
[48] K.R. Hall, L.C. Eagleton, A. Acrivos, T. Vermeulen, Pore and solid diffusion kinetics in fixed-bed adsorption under constant pattern conditions, Ind. Eng. Chem. Fundam. 5 (1966) 212–223.
[49] H.M.F. Freundlich, Uber die adsorption in losungen, J. Phys. Chem. 57 (1906) 385–470.
[50] A. Mittal, J. Mittal, A. Malviya, V.K. Gupta, Adsorptive removal of hazardous anionic dye "Congo red" from wastewater using waste materials and recovery by desorption, J. Colloid Interface Sci. 340 (2009) 16–26.
[51] J.G. Yu, H.G. Yu, B. Cheng, X.J. Zhao, J.C. Yu, W.K. Ho, The effect of calcination temperature on the surface microstructure and photocatalytic activity of TiO_2 thin films prepared by liquid phase deposition, J. Phys. Chem. B 107 (2003) 13871–13879.
[52] J.A. Lewis, Colloidal processing of ceramics, J. Am. Ceram. Soc. 83 (2000) 2341–2359.
[53] S.W. Liu, J.G. Yu, M. Jaroniec, Tunable photocatalytic selectivity of hollow TiO_2 microspheres composed of anatase polyhedra with exposed facets, J. Am. Chem. Soc. 132 (2010) 11914–11916.